A Time Projection Chamber with Micromegas-based Readout

Y. Aoki[i], D. Attié[b], T. Behnke[d], A. Bellerive[a], O. Bezshyyko[s], D.S. Bhattacharya[b,ac], P. Bhattacharya[r,x], S. Bhattacharya[*]retired[r,1], Y. Chang[g], P. Colas[b], G. De Lentdecker[f], K. Dehmelt[d,ab], K. Desch[u], R. Diener[d], M. Dixit[a,t], U. Einhaus[d,v], O. Fedorchuk[d,v], I. Fleck[w], K. Fujii[i], T. Fusayasu[q], S. Ganjour[b], P. Gros[q,z], P. Hayman[a], K. Ikematsu[q,1], L. Jönsson[m], J. Kaminski[u], Y. Kato[k], C. Kleinwort[d], P.M. Kluit[o], M. Kobayashi[i], U. Krämer[d,v,o], B. Lundberg[m], M. Lupberger[u], N. Majumdar[r], P. Malek[d,v], T. Matsuda[i], U. Mjörnmark[m], S. Mukhopadhyay[r], F. Müller[d], A. Münnich[d,y], J. Nakajima[i], S. Narita[h], K. Negishi[h], T. Ogawa[i], A. Oskarsson[m], L. Österman[m], D. Peterson[c], H. Qi[g], M. Riallot[b], C. Rosemann[d], S. Roth[p], P. Schade[d], O. Schäfer[d], R.D. Settles[n], A.N. Shirazi[w], A. Shoji[h], O. Smirnova[m], A. Sugiyama[q], T. Takahashi[e], J. Timmermans[o], M. Titov[b], D. Tsionou[d], A. Vauth[d,v], T. Watanabe[l], U. Werthenbach[w], M. Wu[d,aa], Y. Yang[f], R. Yonamine[f,i], Z. Yuan[g], K. Yumino[i], F. Zhang[j]

[a]*Carleton University, Department of Physics, 1125 Colonel By Drive, ON K1S 5B6, Ottawa, Canada*

[b]*CEA Saclay, Institute of research into the fundamental laws of the Universe (IRFU), Gif sur Yvette, 91191, France*

[c]*Cornell University, Laboratory for Elementary Particle Physics (LEPP), Ithaca, 14853, NY, USA*

[d]*Deutsches Elektronen-Synchrotron DESY, Notkestrasse 85, Hamburg, 22607, Germany*

[e]*Hiroshima University, Graduate School of Advanced Sciences of Matter, 1-3-1 Kagamiyama, Higashi-Hiroshima, Hiroshima 739-8530, Japan*

[f]*Inter University Institute for High Energies (ULB-VUB), Pleinlaan 2, Brussels, 1050, Belgium*

[g]*Institute of High Energy Physics, Chinese Academy of Sciences, 19B Yuquan Road, Shijingshan District, Beijing, 100049, P.R. China*

[h]*Iwate University, 3-18-8 Ueda, Morioka, Iwate 020-8550, Japan*

[i]*High Energy Accelerator Research Organization (KEK), 1-1 Oho, Tsukuba, Ibaraki 305-0801, Japan*

[j]*Hubei University of Technology, 28 Nanli Road, Hong-shan District, Wuchang, Wuhan, Hubei Province 430068, P.R. China*

[k]*Kindai University, Department of Physics, 3-4-1 Kowakae, Higashi-Osaka, Osaka 577-8502, Japan*

[l]*Kogakuin University, Laboratory for High Energy Physics, 2665-1 Nakano-machi, Hachioji, Tokyo 192-0015, Japan*

[m]*Lund University, Department of Physics, Div. of Particle Physics, Box 117, 221 00 Lund, Sweden*

[n]Max Planck Institute for Physics
(Werner Heisenberg Institute), Föhringer Ring 6, Munich, 80805, Germany
[o]National Institute for Sub-
atomic Physics (Nikhef), P.O. Box 41882, 1009 DB Amsterdam, The Netherlands
[p]RWTH Aachen University, Department of Physics,
Institute III B, Otto-Blumenthal-Str,, Aachen, 52074, Germany
[q]Saga University, Department of Physics, 1 Honjo-machi, Saga 840-8502, Japan
[r]Saha Institute of Nuclear Physics, Applied Nuclear Physics Division, 1/AF, Sector 1,
Bidhan Nagar, Kolkata 700064, India
[s]Taras Shevchenko National University of Kyiv, 64/13,
Volodymyrska Street, Kyiv, 01601, Ukraine
[t]TRIUMF, 4004 Wesbrook Mall, Vancouver, BC-V6T-@A3, Canada
[u]University of Bonn, Physikalisches Institut, Nußallee 12, Bonn, 53115, Germany
[v]University of Hamburg, Department of Physics,
Institute of Experimental Physics, Luruper-Chaussee 149, Hamburg, 22761, Germany
[w]University of Siegen, Department of Physics, Emmy Noether Campus, Walter-Flex
Str. 3, Siegen, 57068, Germany
[x]Adamas University, Department of Physics, Adamas Knowledge City, Barasat-Barrackpore Road,
24 Parganas North, Kolkata 700126, India
[y]European-XFEL-GmbH, Holzkoppel 4, Schenefeld, 22869, Germany
[z]Queen's University, Department of Physics, Engineering Physics & Astronomy, Stirling Hall,
64 Bader Lane, Kingston, Ontario K7L 3N6, Canada
[aa]Radboud University, Institute for Mathematics, Astrophysics and Particle Physics, P.O. Box 9010, 6500 GL Nijmegen, The Netherlands
[ab]State University of New York at Stony Brook,
Department of Physics and Astronomy, 100 Nicolls Road, Stony-Brook, 11794-3800, NY, USA
[ac]University of Würzburg,
Institute for Theoretical Physics and Astrophysics, Am Hubland, Würzburg, 97074, Germany

Abstract

In this paper we present the proposal and development of a Micromegas-based readout Time Projection Chamber (TPC) designed for central tracking within the framework of the International Large Detector (ILD), a detector concept for the International Linear Collider (ILC) concept. Prototype modules were constructed and subsequently exposed to beam tests, aiming to validate the design of the Micromegas-based readout featuring a resistive anode. These tests were conducted at the DESY Test Beam facility, which includes a 5 GeV electron beam and a field cage equipped with ancillaries, specifically designed for the Linear Collider TPC (LCTPC) collaboration. The results of these beam tests are detailed, and their implications are extrapolated to project the performance of a Micromegas-based readout TPC within

the envisioned operational conditions of the future Linear Collider.

Keywords:

1. Introduction

The LCTPC collaborationLCT was established with the mission to design and investigate a high-performance Time Projection Chamber (TPC) tailored for physics exploration at the future e^+e^- International Linear Collider, reaching center-of-mass energies up to 1 TeV. Within the collaboration, various micro-pattern gaseous detectors (MPGD) technologies for a pad-based readout in a TPC are being explored. These include the Gas Electron Multiplier (GEMs)Sauli (1997) and the Micro Mesh Gaseous Detectors (Micromegas)Giomataris et al. (1996). Additionally, there is a proposal to integrate a high-density pixelized CMOS ASIC (Medipix2/Timepix) with a GEM or Micromegas gas amplification stageColas et al. (2004).

In the early 2000s, several small Time Projection Chamber (TPC) prototypes were constructed to investigate different aspects of Multi-Wire Proportional Chamber (MWPC), GEM, and Micromegas readout technologies. Measurements were conducted on ion feedback and spatial resolution across various gas mixtures. The findings revealed that the MWPC readout was not a viable fallback solution for the ILC TPC, as its spatial resolution was significantly compromised by $\mathbf{E} \times \mathbf{B}$ effects in the proximity of the wire planesAckermann et al. (2010). On the contrary, a pivotal demonstration affirmed that a TPC with a MPGD readout could maintain stable operation and successfully meet the design objective of achieving a spatial resolution of 100 μm under a strong axial magnetic field of 3.5 T. Furthermore, simulations, corroborated by a beam test, revealed that the resolution target could not be attained with a Micromegas featuring millimetric pads. This limitation arose from the excessive localization of the avalanche, hindering the formation of a reliable barycenter Arogancia et al. (2009). Consequently, the imperative for charge spreading was established, leading to the development of a method based on a continuous resistive-capacitive network covering the anode array of pads

Recent findings from a TPC prototype, positioned in a 1T solenoidal field and equipped with three independent GEM-based readout modules, have been reported in Attie et al. (2017). This paper provides a comprehensive overview of the investigation involving a TPC with a Micromegas-based readout designed for the ILD conceptBehnke et al. (2020). The subsequent sections introduce the prototype and the test beam facility at DESY, outline the reconstruction methods employed, and present the outcomes of the test beam campaign.

2. Setup and Data Taking

2.1. The DESY test beam facility

Since 2008, the LCTPC collaboration has consistently conducted beam tests with a Large Prototype TPCBehnke et al. (2010). This prototype, an integral part of the EUDETEUD and AIDAAID projects, serves as shared infrastructure and is situated at the DESY II facilityDES. The facility encompasses a 1.2 T solenoidal superconducting magnet (equivalent to 0.2 radiation lengths) mounted on a movable table, complete with cosmic-ray and beam trigger systems, a gas distribution system, a Very High Voltage supply (up to 30 kV), and a field cage measuring 580 mm in length and 720 mm in diameter.

The Large Prototype was specifically designed to assess various readout technologies, including Micromegas, GEMs, and TimePix. Focusing on the Micromegas technology, 10 data-taking periods were conducted between 2008 and 2018. Notably, results based on a single module in 2010 demonstrated a remarkable 60 μm rϕ resolution at zero drift distanceWang (2013), showcasing the effectiveness of the technology with 3 mm wide pads.

2.2. Layout

This paper presents results from the 2015 and 2018 data-taking periods, involving 7 and 4 modules, respectively. The 7-module run aimed at evaluating the construction and operation of a multi-module configuration, featuring a 2-phase CO_2 cooling system for the electronics. The configuration and numbering of the 7 modules are shown in Fig. 1, showcasing a charged track traversing three Micromegas modules. Notably, the drift distance covers approximately 50cm under a magnetic field strength of 1T.

In the 4-module run, modules 0, 3, 5, and 6 (as per the module numbering in Fig. 1) were chosen, facilitating tracks that traverse three modules. This run benefited from enhanced mechanics, enabling pad connections to electronic channels with an exceptional efficiency of 99.9%. Only 8 out of 6904 channels exhibited faulty electric contact, as two pads per module were utilized for connecting the mesh to ground or high voltage.

Furthermore, this run served as a test to evaluate a lightweight space-frame endplate. These multi-module runs provided an opportunity to conduct a comprehensive study on track distortions.

2.3. Module description

A keystone shape was selected for the modules to explore the complexity introduced by covering the circular endplate with concentric rows of modules. For

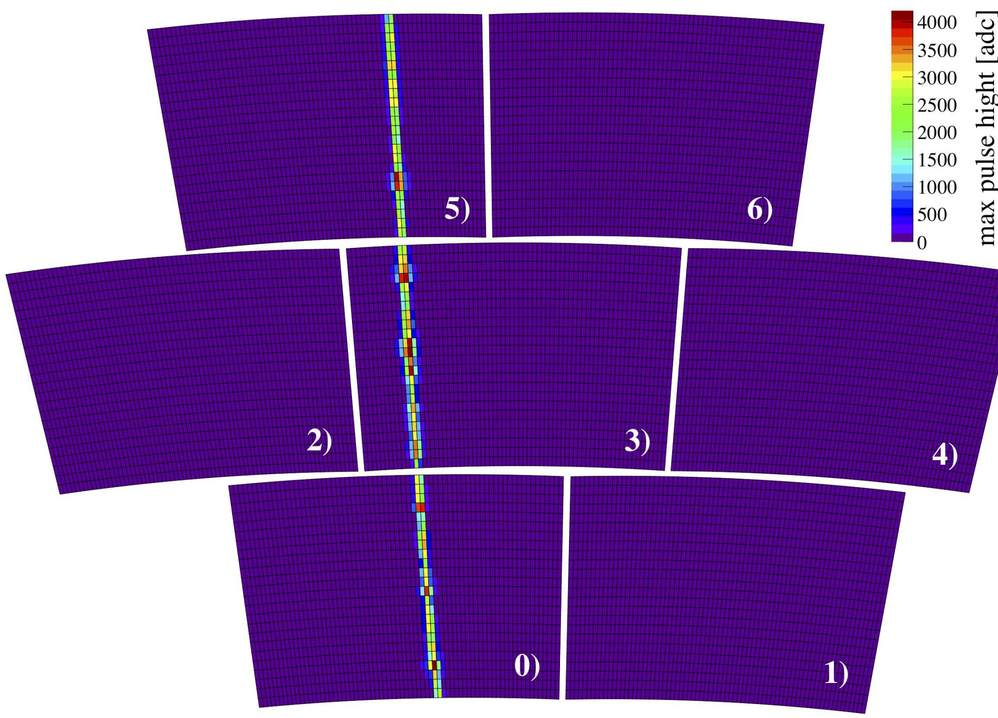

Figure 1: A typical beam event display showing a charged particle traversing three ERAM modules.

simplicity, all seven modules are identical, featuring an inner radius of 1430 mm and an outer radius of 1600 mm. The readout pad plane is divided into 24 circular rows, each containing 72 copper pads (refer to Fig. 1 for a sketch). The pads measure 7 mm in length along the radial coordinate, while their width varies from 2.7 to 3.2 mm from the innermost to the outermost layer. These 24x72 pads are connected through the PCB to twelve 300-point zero-force connectors. Six front-end cards, each equipped with four AFTER ASICs, are securely mounted on a stiffener. Each ASIC channel includes an amplifier-shaper. The signals are digitized by a 12-bit ADC, sampled using a Switched Capacitor Array with a depth of 511 time bins (at a frequency of 25 MHz for most of the collected data), consolidated, and transmitted via an optical link to the computer.

The PCB is insulated with a 75 μm-thick layer, on top of which a Diamond Like Carbon (DLC)-coated kapton layer with a resistivity of 2.5 Mohm/sq is applied. This stack forms a continuous resistive-capacitive circuit that disperses the deposited charge across the pad array. In the Encapsulated Resistive Anode Micromegas (ERAM) configuration, a copper frame connects the border of the DLC layer to the high voltage potential. Gas amplification is achieved with a Micromegas fixed onto the PCB using the 'bulk' technology, with a gap of 128 μm.

In 2018, four ERAM modules were produced and subjected to testing. However, due to chemical runs occurring on the DLC layer after the application of the resistive sheet, the anode surfaces of the modules did not exhibit uniform quality. The module with the most favorable surface condition was positioned at the center and selected for the resolution study.

2.4. Data taking

The gas employed during these data collection periods consisted of a mixture of Argon, CF_4, and isobutane in respective proportions of 95:3:2 by volume, flowing at a rate of approximately 50 l/hour. Oxygen content in the gas was continuously monitored and measured to range between 20 and 30 ppm in 2015, and below 60 ppm in 2018. Water content was measured using a dew-point method and found to be around 120 ppm for most of the operational duration.

In the majority of the collected data, the electron beam was parallel to the anode plane with a momentum of 5 GeV/c. The beam had a diameter of 4 mm r.m.s., thereby covering approximately 3 pads. The trigger rate ranged from a few hundred Hz to 2 kHz, while the data acquisition rate was approximately 40 Hz, constrained by the readout time. Pedestals were subtracted online in the majority of runs. A total of 20,000 tracks were recorded at various z positions (every 50 mm), amplification voltages, peaking times, x positions of the beam, and azimuthal angles. Additionally,

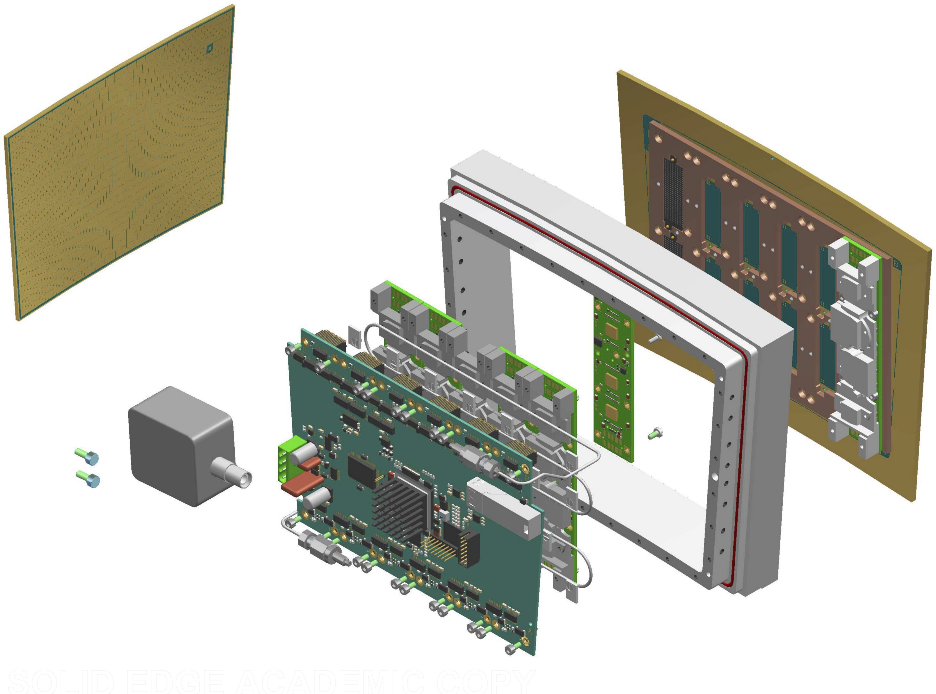

Figure 2: The layout of a Micromegas module. A stainless-steel stiffener serves as a robust reference for 300-point connectors, ensuring the Front End Cards remain in their correct positions.

data were collected at B=0 T for alignment purposes. During analysis, only events with a single track were considered, resulting in the rejection of approximately 50% of the events.

The parameters of the readout electronics were selected as follows: a sampling frequency of 25 MHz, amplifier chain sensitivity of 30 fC per ADC channel, and peaking times of 100 ns, 200 ns, 400 ns, 500 ns, and 600 ns.

The modules were effectively cooled using a flow of CO_2 under 50 bars, circulating through 1 mm inner diameter steel pipes. Temperature monitoring of the Front-End Cards and the Front-End Mezzanine was conducted using probes installed on the boards. The temperature was successfully reduced from 60 degrees to 30 degrees.

During the 2015 7-module setup, each module had an independent cooling loop, allowing for the closure of circulation in any module in the event of a leak. Conversely, in the 2018 4-module setup, a single loop was employed to cool all four modules.

3. Event Reconstruction

The reconstruction of events and analysis of detector performance were conducted using the MarlinTPC software package Vogel et al. (2007), built upon the linear collider software framework Gaede (2006); Gaede et al. (2003). The event reconstruction involves several steps, including pulse finding, hit reconstruction via calibration of the pad response function (PRF), track finding and fitting, and bias correction.

The analysis pipeline is applied to each run individually. Initially, pad amplitude and arrival time are computed from shaped pulses of each pad. These pulses are then aggregated into row-based clusters (hits), enabling calibration of the Pad Response Function (PRF) for the specific run. In the absence of external track measurements, the absolute position is estimated and corrected through an iterative process involving PRF calibration and geometric corrections.

Once the hits are constructed, along with their positions on the pad plane, timing, and total charge, bias corrections are derived for each pad row in the detector. Subsequently, after all necessary corrections have been applied, track finding and fitting algorithms are employed to calculate the detector's resolution.

3.1. Hit reconstruction

Electrons generated in the drift volume of the TPC drift towards the anode. Passing through the gap between the MM mesh and the anode, they trigger an avalanche amplification process, generating a charge cloud. This cloud then drifts from the mesh towards the pad plane. Due to the narrow gap between the mesh and the anode, the width of this cloud is significantly smaller than the width of the pad.

The selection of the RC values of the resistive anode is designed so that, on average, more than three pads in each row detect a signal from the charge dispersion across the 2D continuous RC network. These individual signals registered on the pads are referred to as pulses. Subsequently, a row-based clustering algorithm is employed to group several adjacent pulses within a pad row into a cluster, referred to as a hit.

The electronic noise is evaluated individually for each pad during dedicated runs recorded without beam. The mean of this noise defines the pedestal, while the width of the noise determines the threshold, typically set at 4.5 σ, for zero suppression in the readout electronics.

Any dispersed charge exceeding this threshold on individual pads is digitized at a sampling frequency of 25 MHz. To capture the complete time evolution of the signal, 13 time bins before and 12 time bins after the second threshold crossing are stored. Pulsed signals from neighboring pads within a row are combined into a single hit if they fall within a time window of 1 μs relative to the time of the largest pulse. The charge of each pulse is calculated as the ADC counts in the maximum bin across the entire range.

To estimate the track position, the relative fraction of charge observed by pads is fitted using the Pad Response Function (PRF) Dixit et al. (2004). However, this initial estimation is subject to bias due to non-uniformities in the anode RC-network and geometric effects of electric and magnetic fields at the anode plane. In the absence of external track measurements, an iterative process of PRF calibration is employed. This process begins with an initial guess of the PRF parameters and relies on the internal consistency of the data to ensure the selection of an appropriate PRF.

The PRF is characterized as the normalized charge (Q/Q_{max}) plotted against the track position x_{track} relative to the pad position x_{pad}. Its parametrization involves a combination of Gaussian and Lorentzian functions, as introduced in Shiell (2012), defined as follows:

$$\mathrm{PRF}(x, r, w) = \frac{\exp\Big(-4\ln(2)(1-r)\dfrac{x^2}{w^2}\Big)}{1 + \dfrac{4rx^2}{w^2}} \tag{1}$$

Here, $x = x_{\mathrm{track}} - x_{\mathrm{pad}}$, while r and w denote mixing and width parameters, respectively. Fig. 3(left) illustrates the typical distribution of the Pad Response Function (PRF) under a drift field of 230V/cm and a drift distance of 50mm. The magnitude of charge dispersion is determined by fitting it with the function defined in Eq. (1). The half-width at half maximum (FWHM) of the PRF measures approximately 1.7 mm, although this varies depending on the pad's location on the PCB.

Fig. 3(right) displays a map of the FWHM of the fitted PRF. This non-uniformity arises from the manufacturing process of the resistive surface via sputtering and could potentially be improved in future production iterations.

The hit's time is determined by the largest pulse within it, identified from the inflection point on the rising edge of the pulse. This inflection point is derived from fitting the rising edge of the signal. Time information from neighboring pulses is disregarded as they consistently occur later than the central pulse, attributed to charge dispersion in the resistive anode. The hit's charge is computed by summing the charges of all pulses contributing to it.

3.2. Track reconstruction and selection

The track finding process relies on reconstructed hit information and employs an iterative triplet algorithm Kleinwort (2014). Hits situated in adjacent rows are grouped into triplets. Each triplet within a module forms a segment corresponding

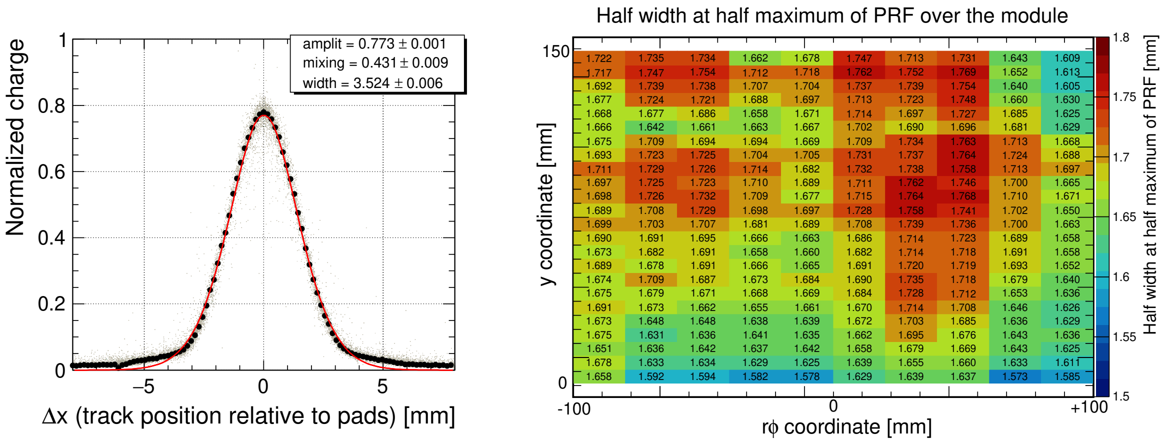

Figure 3: (Left) Normalized charge as a function of x at a drift field of 230 V/cm and a drift distance of 50 mm. The red curve represents the fitted PRF defined in Eq. (1). (Right) Fitted half-width at half maximum (HWHM) of the PRF across the central module at a drift distance of 50 mm.

to that module, taking into account the position and direction of each triplet. These segments are then merged across modules to construct a track candidate.

While several track fitting algorithms are available in the MarlinTPC framework, they yield nearly identical results regardless of the presence or absence of a magnetic field, owing to the low material budget Mueller (2016). Specifically, a straight-line model is used for data acquired at 0 T magnetic field, whereas a helix model is applied for data collected with a magnetic field. Track parameters are determined by fitting all identified hits assigned to a track. Further details on the reconstructed track parameters can be found in Kraemer (2006).

Combining all three modules allows for a maximum of 72 hits to be reconstructed on a single track, corresponding to the number of rows crossed by a track. Notably, the modules installed into LP1 feature no dead pads within the fiducial area of passing tracks. To ensure high-quality reconstruction, only tracks with the maximum number of rows, including both the innermost and outermost rows, are considered. For further refinement, only tracks falling within the range of [-0.04,$+0.02$] radians in local ϕ impact angle are included in the analysis. This range corresponds to a 2.5σ deviation around the peak of the ϕ distribution. Additionally, events containing more than one reconstructed track are excluded from the analysis to avoid contamination by tracks originating from interactions with the magnet or field cage wall. Occasionally, pulse charge saturation occurs due to the relatively large contribution of δ-rays. However, tracks containing hits composed of saturated pulses are not excluded from the analysis to prevent overestimation of the real detector's performance. Unless stated otherwise, no further selection criteria are applied in the subsequent analyses.

3.3. Bias correction

Local inhomogeneities in the construction of the resistive anode assembly introduce position-dependent systematic biases in each row. While the PRF effectively accounts for real charge distribution and mitigates S-curve effects, residual oscillations of approximately 100 μm periodically occur when using the PRF position estimator. Consequently, localized variations in resistive anode properties result in systematic errors in track position measurement.

To address this issue, biases are quantified and corrected before calculating resolution. Row-by-row corrections, represented by average residuals, are computed relative to the distance from the center of the leading pad normalized to the pitch w.

Fig. 4 illustrates the typical residual distribution as a function of $(x - x_{pad})/w$, showcasing the effectiveness of the bias corrections.

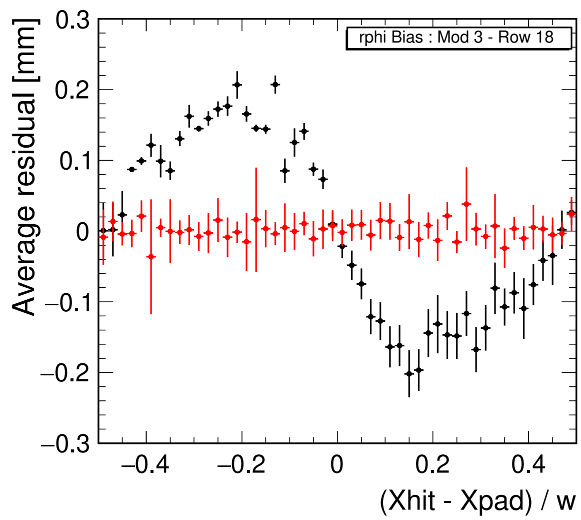

Figure 4: Residuals plotted against the distance between the hit and the center of the pad, expressed in units of pad width, $(x - x_{pad})/w$. Black and red dots represent the data before and after bias corrections, respectively. This plot illustrates the distribution for module 3 and row 18 at a drift distance of 50 mm, with similar distributions observed across other rows.

3.4. Module alignment

For module alignment, track parameters are extracted using a General Broken Lines (GBL) fit Kleinwort (2012, a), a method mathematically equivalent to a Kalman filter. The GBL approach enables direct utilization of the Millepede II Blobel (2006); Kleinwort (b) toolkit for track-based alignment and calibration. In the case of data taken at a 0 T magnetic field, a straight line is employed as the track model.

To optimize statistical precision, alignment primarily relies on data satisfying stringent track quality criteria, recorded under 0 T magnetic field conditions. Millepede II conducts an iterative minimization of the track χ^2 concerning rotations and translations of the modules, with the central module serving as a reference. Only tracks traversing all three modules are considered, while the three inner and outermost pad-rows are excluded from the GBL track fit to mitigate biases stemming from local field distortions. Accurate determinations are achieved for translations along rϕ and rotations around the z-axis. Notably, our alignment algorithm is insensitive to translations along the z-direction or the beam direction. The iterative procedure continues until all alignment parameters fall within their uncertainties.

Table 1 illustrates the convergence of alignment parameters for the upper and bottom modules after four iterations. It is essential to note that, although the modules are assumed to be flat, metrological measurements suggest a potential sagging of up to 200 μm.

Table 1: The table presents alignment correction parameters after the first and fourth iteration. Each set of parameters is applied to update the geometry model in the corresponding iteration.

parameter		1st-iteration	2nd-iteration	4th-iteration
module0[1)]	Δx [μm]	-763.8 ± 9.5	-37.6 ± 9.4	0.8 ± 9.4
module0	Δy [μm]	143.8 ± 7.9	-83.4 ± 7.3	1.2 ± 7.4
module0	Rot z [μrad]	-85.8 ± 4.9	51.0 ± 4.6	-1.0 ± 4.6
module5[1)]	Δx [μm]	1004 ± 9.5	111.1 ± 9.4	-20.0 ± 9.5
module5	Δy [μm]	-1929 ± 6.7	30.2 ± 6.7	-8.5 ± 6.7
module5	Rot z [μrad]	1515 ± 4.7	-11.5 ± 4.6	5.1 ± 4.7

[1)] Module 0 and Module 5 denote the modules installed in the upper and lower positions, respectively, relative to the central module.

4. Results

4.1. Reconstruction efficiency

The reconstruction efficiency of a track-associated hit is evaluated for each pad row to assess the detector's response and the overall reconstruction chain. The efficiency is defined as follows:

$$\text{efficiency} = \frac{\text{Number of actual hits}}{\text{Number of expected hits}} . \quad (2)$$

To estimate the "Numberofexpectedhits" for a specific pad row, the corresponding row is excluded from the reconstruction chain. Fig. 5 illustrates the hit reconstruction efficiency of each pad row for tracks traversing parallel to the pad row, at two different drift lengths of 35 mm and 555 mm under a magnetic field of 1 T.

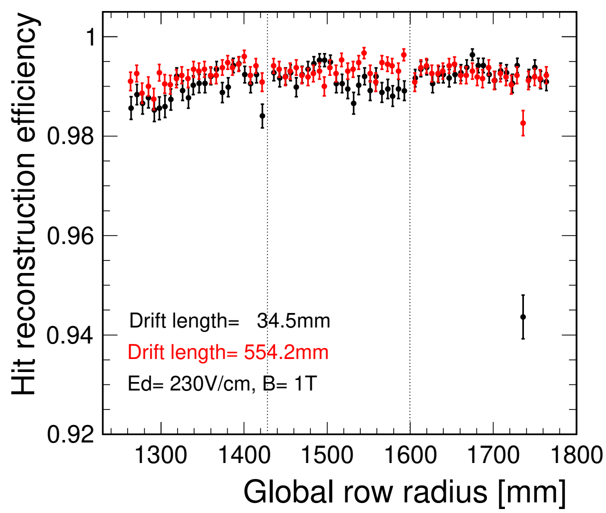

Figure 5: The hit reconstruction efficiency along a track crossing three Micromegas modules. Black and red points represent data at drift lengths of 35 mm and 555 mm, respectively. Small drops correspond to the locations of the pads connected to the mesh.

A significant dip is observed near the last row, attributed to the presence of pads with externally provided potential. Some minor degradation in reconstruction efficiency is noted in pad rows located closer to the module's outer edge, although this effect is relatively small compared to other pad rows and falls within statistical error margins. This may arise from the considerable distortion of the electric field caused by misalignment between the module and the outer field cage, as will be discussed later.

The reconstruction efficiency of track-associated hits for the longer (shorter) drift distance averages at $99.3 \pm 0.2\%$ ($99.1 \pm 0.2\%$) across all three Micromegas modules, without excluding any pad rows.

4.2. Drift velocity

Prior to evaluating the detector's performance, it is essential to estimate reference parameters including the zero-drift time t_0, the initial position of the moving stage z_0, and the drift velocity v_{drift}. These parameters, along with their respective errors, are utilized as inputs for the subsequent studies.

To determine t_0 and z_0, hit time measurements were conducted for two drift field configurations. These measurements yielded drift velocities and a single intersection point corresponding to the zero-drift time t_0 and the initial position of the moving stage z_0. Fig. 6 illustrates the relationship between the positions of the moving stage and the mean values of the hit time measured with the central module. Table 2 summarizes the measured values of t_0, z_0, and v_{drift} in different run periods, along with simulated values obtained using Garfield^{++}Veenhof, which interfaces with Magboltz version 9.0.1Biagi (1999).

The drift velocities observed in the measurement and simulated with consistent gas properties exhibit a good agreement. Additionally, each t_0 and drift velocity estimated by different modules are consistent within their respective statistical errors. The table also includes D_t and D_l, denoting the transverse and longitudinal diffusion constants, respectively. These values are crucial for extracting detector parameters

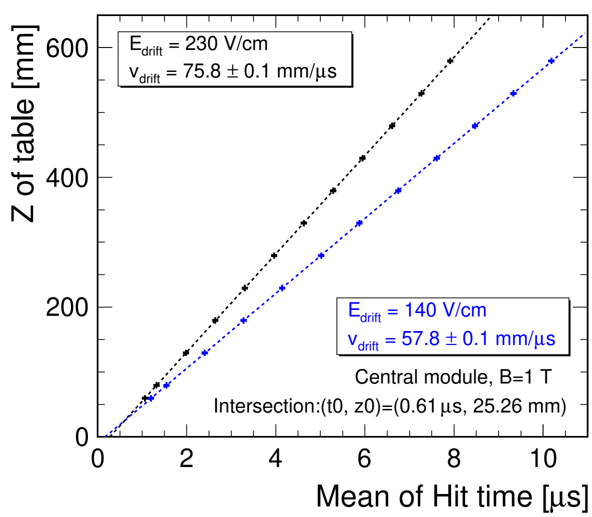

Figure 6: The plot illustrates the calibration of the relationship between the position of the moving table and the arrival time of ionized charges at the module. The intersection point provides the timing of the zero-drift.

Table 2: The table presents the estimated reference parameters and drift velocity measured with the central module in various run periods, along with the corresponding gas conditions provided below. E_d denotes the set value for the drift field. v_{sim}, D_t, and D_l represent simulated values obtained using Magboltz version 9.0.1 Biagi (1999).

B[1)]	z_0	t_0	E_d	$v_{\mathrm{drift}}^{\mathrm{meas}}$	$v_{\mathrm{drift}}^{\mathrm{simu}}$[2)]	D_t, D_l[3)]
[T]	[mm]	[μs]	[V/cm]	[mm/μs]	[mm/μs]	[μm/$\sqrt{\mathrm{cm}}$]
1	25.3±3.0	0.61±0.05	140	57.78±0.10	57.7	74.9, 309
			230	75.75±0.13	75.5	93.6, 230.0
0	27.4±3.0	0.65±0.05	140	57.98±0.10	57.2	309, 309
			230	75.85±0.13	75.2	308, 230

[1)] Conditions during the data taking : temperature: 16 °C, system pressure: 1015 hPa, H_2O: 100 ppm, O_2: 60 ppm.

[2)] Statistical errors are negligible.

[3)] Statistical errors are at the 1% level.

4.3. rϕ *and z resolution*

The track reconstruction, as detailed in the previous section, was carried out for both scenarios: using only the central module and combining all three modules, allowing for a comparison of module dependencies. Additionally, track selection criteria were applied following the descriptions provided earlier.

Fig. 7 (left) shows the spatial resolution $\sigma_{\mathrm{r}\phi}$ at a short drift distance of about 50 mm as a function of the potential difference ΔV between the resistive anode and the micro-mesh. It's evident that both too small and too large potential differences lead to degraded spatial resolution due to inadequate avalanche charge or an increase in the number of saturated pulses associated with hits from tracks. At a ΔV of 380 V, approximately 13.9±0.6% of all pulses included in the hit are saturated. A ΔV of around 370 V appears to be optimal for detector operation with T2K gas, corresponding to a gas gain of roughly 1800 Wang (2013). The ratio of saturated pulses with a ΔV of 370 is approximately 4.6±0.4%. Although 360 V also seems to be suitable, a larger ΔV is chosen for operation to minimize gas gain fluctuation, which decreases with larger electric fields according to simulations Zerguerras et al. (2015).

In Fig. 7 (right), the rϕ and z resolutions at a short drift distance of about 50 mm are plotted against the peaking time. At smaller peaking times, amplifier noise tends to be higher and the collection efficiency of electrons decreases, resulting in a slight improvement in the rϕ resolution with larger peaking times. As the width of the time distribution is proportional to the shaping time, the z resolution shows a linear increase with the peaking time.

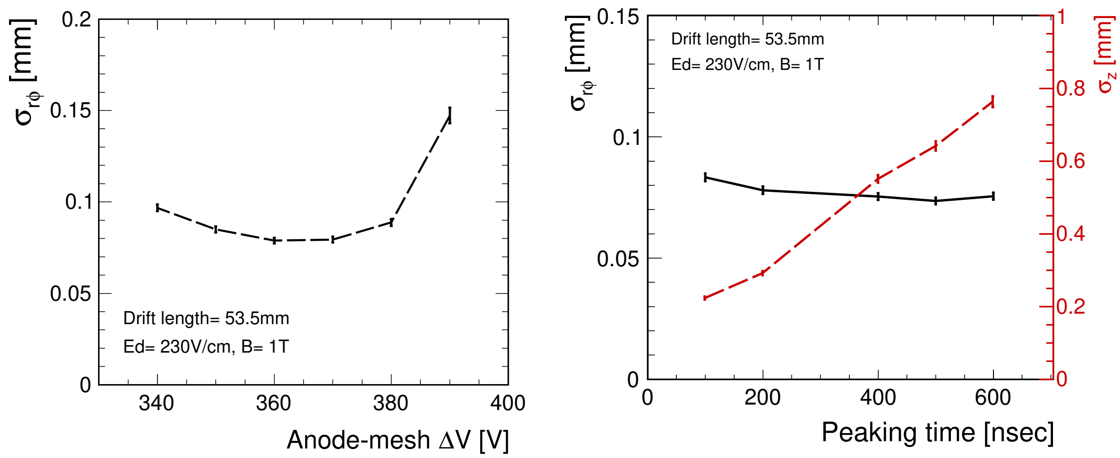

Figure 7: Left: Spatial resolution as a function of the potential difference ΔV between the resistive anode and micro-mesh. Right: Dependence of the $r\phi$ and z spatial resolution on the peaking time of the electronics.

As described in a later paragraph, the innermost few pad rows on the lower module and a couple of central pad rows on the upper module exhibit relatively worse spatial resolution. This is attributed to both misalignment of electrodes within the field cage and the inhomogeneity of the resistive anode. Therefore, for performance estimation, only the central module is considered.

Fig. 8 and Fig. 9 show the spatial resolution $\sigma_r\phi$ and z resolution σ_z for drift fields of 140 and 230 V/cm, respectively, at magnetic fields of 0 and 1 T. Each drift length is determined by measuring hit time and propagating its error: $z_{\text{measure}} = (t_{\text{measure}} - t_0) \cdot v_{\text{drift}}$. Each data point represents the average value of all 24 pad-rows in the module. The overall behavior of the resolutions is fitted with the following asymptotic resolution function, which can extract parameters describing the detector performance.

$$\sigma^2_{r\phi/z} = \sigma^2_{r\phi 0/z0} + \frac{D^2_{t/l}}{N_{\text{eff}}} \cdot z \tag{3}$$

Here, D_t and D_l represent the transverse and longitudinal diffusion constants, respectively, while N_{eff} denotes the effective number of electrons contributing to the coordinate measurement. $\sigma_{r\phi 0/z0}$ are constant terms influenced by electronic noise,

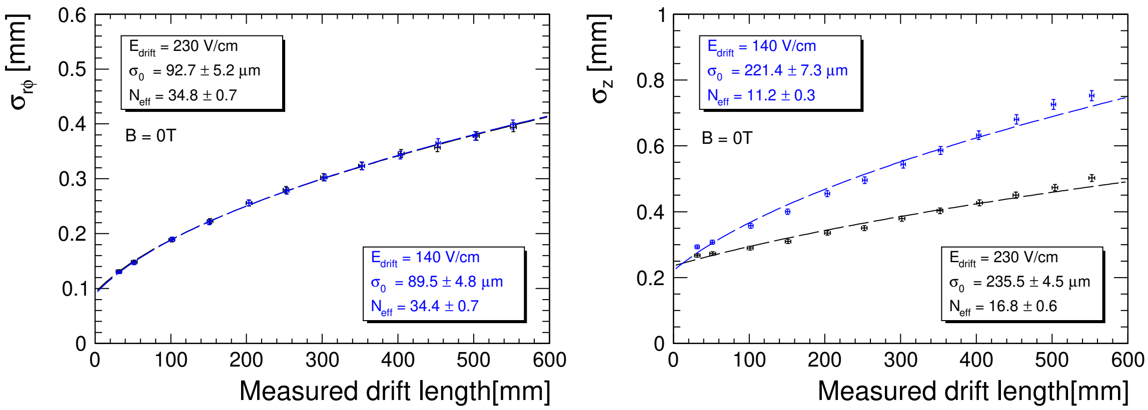

Figure 8: The $r\phi$ and z resolution as a function of the measured drift length, for B=0 T. The black and blue colors show two different drift fields of 140 and 230 V/cm. The points are an average over 24 pad rows of the central module.

finite mesh pitch, and delta rays. At B=0, the contribution from delta electrons increases due to long-range emission from the track. Thanks to charge dispersion and a low electronic threshold, each hit typically involves more than three pads per row, even at the shortest drift lengths.

In Fig. 8 (left), the overlapping resolution for the two drift field values is attributed to the fortuitous equality of the diffusion constant for these fields at B=0. It's worth noting that the fit quality is not perfect at large drift distances, especially at B=0, possibly due to electron loss resulting from the exclusion of side pads in the time determination.

The estimated N_{eff} for both fields are 22.7 and 24.7, respectively, which align well with values obtained from numerical simulations Kobayashi (2006), suggesting N_{eff} with argon-based gas to be within the range of 22–28. However, it's important to note that the fitted functions do not perfectly align with the data, particularly at long drift distances, indicating that the given N_{eff} may be slightly underestimated. This discrepancy suggests that the resolution distribution with the charge dispersion technique cannot be fully described by the simple asymptotic function due to factors such as entanglement of dispersion and threshold effects.

The z resolution shows good agreement with the data across the measurement range. N_{eff} for the field of 230 V/cm is 27.7, which is nearly consistent with the $r\phi$ resolution. However, for the field of 140 V/cm, N_{eff} is half compared to that of 230 V/cm. This discrepancy suggests that not all charge in the corresponding pad-row is utilized for time estimation due to the larger diffusion constant and the time estimator method, which employs the Gaussian inflexion method by fitting the rising

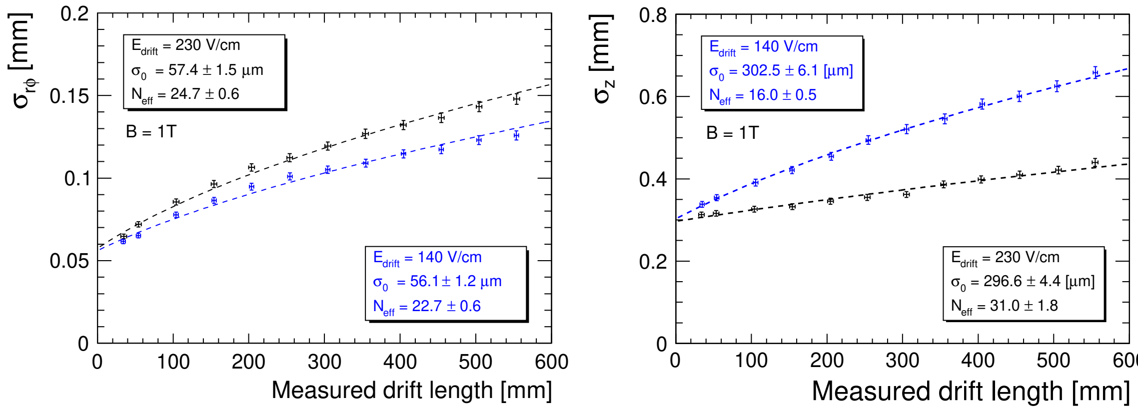

Figure 9: The $r\phi$ and z resolutions plotted against the measured drift length, with B=1T. The black and blue colors represent two different drift fields of 140 and 230 V/cm, respectively. The points represent averages over 24 pad rows of the central module.

edge of the pulse. The smaller N_{eff} in this case implies a difference in the number of primary electrons used for time estimation.

The two plots depicted in Fig. 10 show the spatial and z resolutions in each pad row with track reconstruction using three modules. It's evident that the spatial resolution at the module boundary deteriorates relatively due to charge loss arising from distortion of the electric field. The innermost rows, facing the electric strips of the field cage, are significantly impacted by misalignment of the module towards the strips along the z direction. Additionally, in the outermost module, the spatial resolutions in the central pad-rows suddenly drop. This could be attributed to the inhomogeneity of the charge dispersion, as observed in the HWHM of the charge spread distribution of the corresponding pad-row. In contrast, the z resolution maintains a flat response across the modules.

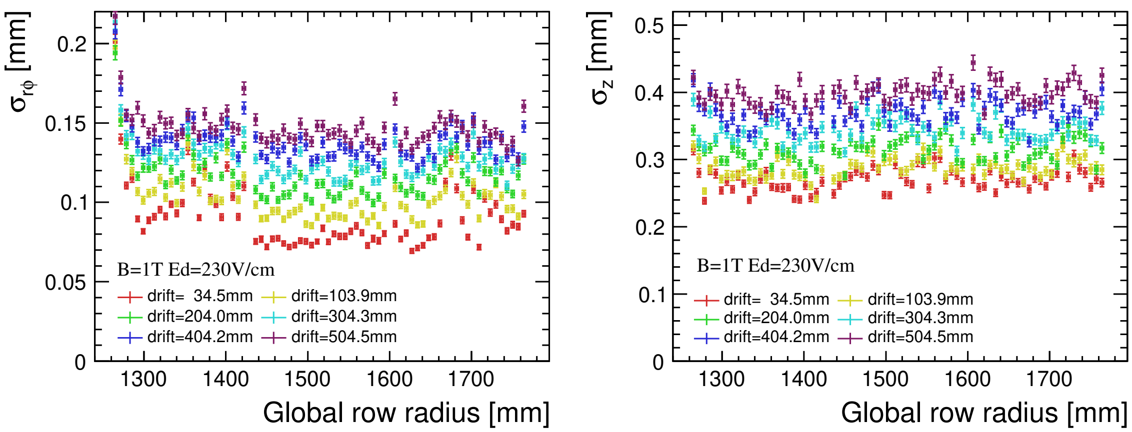

Figure 10: The spatial (left) and z (right) resolutions for various drift lengths across all pad-rows in three modules, utilizing tracks reconstructed within those modules.

4.4. rϕ *and z distortion*

One of the primary motivations behind the latest test beam campaign was to demonstrate that the new high-voltage (H.V.) scheme, known as the encapsulation H.V. scheme, can effectively reduce track distortions. Fig. 11 and Fig. 12 show the behaviors of track distortion in $r\phi$ and z coordinates across the pad-rows. The distortions, denoted as $\Delta_{r\phi/z}$, are defined as the residuals between a track and the hit position associated with that track: $\Delta_{r\phi/z} = \text{trackr}\phi/\text{z} - \text{hitr}\phi/\text{z}$.

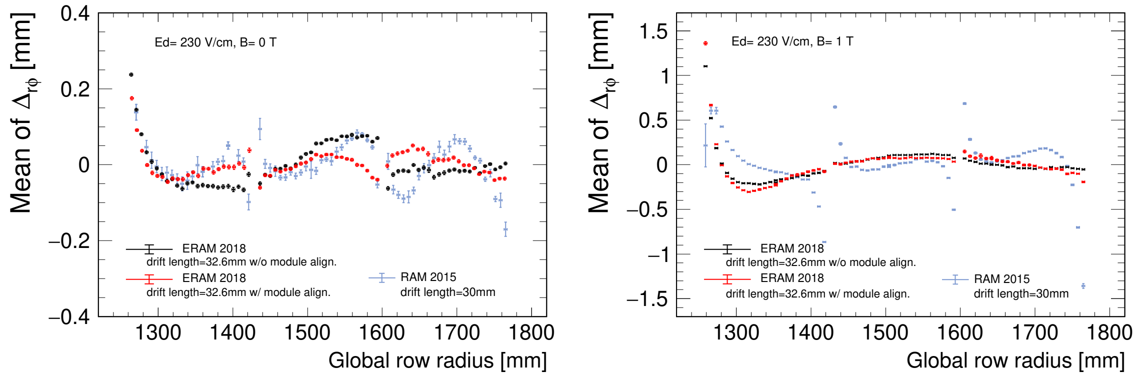

Figure 11: The plots display the mean residual in rϕ across three modules, plotted against the row radius. Left: B=0, Right: B=1 T.

Fig. 11 shows the distortion of $\Delta_{r\phi}$ under magnetic fields of 0 and 1T, demonstrating the application of module alignment in the data as well. To highlight the encapsulation scheme, results from the 2015 beam test campaign at DESY with standard resistive-anode MicromegasBhattacharya (Date: 10/12/2015,D) are overlaid on the plots. In the 2018 data at B=0T, module alignment corrections have smoothed out the distortions at module boundaries, although some residual distortions remain due to slight module deformation. The improvement in track distortion under the 1T magnetic field is significant, with a reduction factor of 20 from the 2.0 to 0.1 mm level at the module boundaries.

Fig. 12 similarly depicts the track distortion in z. The magnitude of the distortion near the module boundaries is reduced from approximately 2.0 mm to 0.5 mm level.

Even with the ERAM module in 2018, the distribution exhibits a mountain-like shape over the module. This shape may arise from slight deformation of the module toward its center, as well as field distortion around the module boundary. The former leads to an enlarged drift distance in the central part, resulting in lower electric field strength and slower drift velocity. The latter causes distortion of electric field lines, compelling drifting electrons to cover a longer distance. Consequently,

Δ_z demonstrates the mountain shape. Untangling these overlapping influences is challenging, and a dedicated study is necessary.

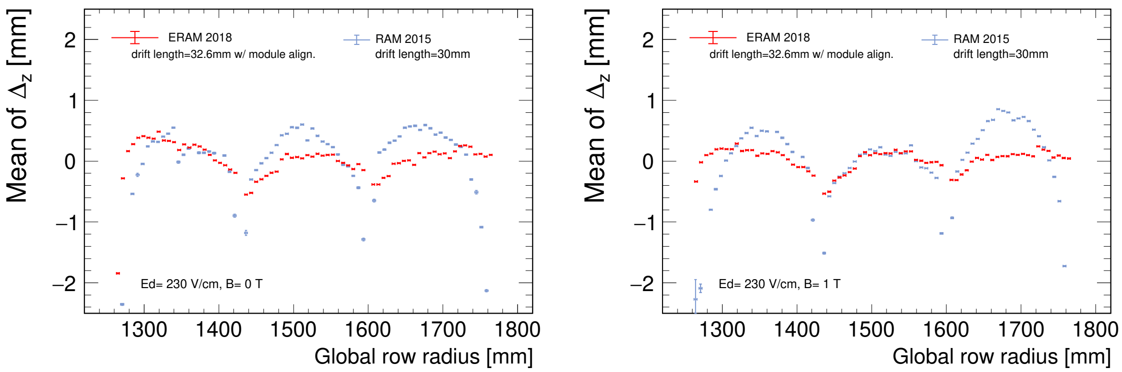

Figure 12: The mean residual in z across the three modules. On the left is B=0, and on the right is B=1 T. The data from 2015 is represented in blue, while data from 2018, with the new grounding scheme, is depicted in red.

4.5. dE/dx Resolution

The charge generated by primary electrons is accumulated per pad-row and aggregated into a hit. This leads to a hit charge distribution resembling a Landau function, commonly known as a straggling function. Because of its asymmetric nature, the direct mean value <dE/dx> of the distribution is not an ideal estimator for energy deposition. Therefore, the hit charge distribution is symmetrized through truncation, a method traditionally referred to as truncated mean. The dE/dx resolution is then defined as $\sigma_{<\mathrm{dE/dx}>}/<\mathrm{dE/dx}>$, assuming a Gaussian-like distribution.

To determine the optimal truncation, the dE/dx resolution is evaluated while varying the percentage of truncation. Empirically, truncating the highest 30% and retaining the lowest 70% yields the best dE/dx resolution. Since gas gain variation from pad-row to pad-row across the detector does not impact the resolution, gain correction is unnecessary Shoji (2018). Furthermore, it is observed that the resolution remains unaffected by drift length under conditions of minimal diffusion, where the charge localization is significantly smaller compared to the pad height.

To accommodate a larger TPC size with a substantial number of hits and to estimate the dE/dx resolution, extrapolation was performed by connecting tracks across a few events until a sufficient number of hits were utilized. Fig. 13 illustrates the dE/dx resolution as a function of the track length, derived from a single run comprising 10,000 events. A power-law function is fitted to the data points, revealing an exponent parameter κ consistent with -0.5. This observation suggests that the overall behavior closely aligns to the statistics of the number of independent samplings. The achievable dE/dx resolution for a Micromegas-TPC with an arm length of 1440 mm and a pad height of 7 mm is determined to be 4.82 ± 0.41 %.

4.6. The track angle effect

In the context of Linear Collider applications, our primary objective is to achieve the utmost point resolution for radial high-momentum tracks emanating from the interaction point. In the radial alignment of pads, these tracks are perpendicular to the pad rows. Nonetheless, the resolution experiences degradation when the local angle between the pad axis and the track deviates from 0, owing to cluster size fluctuations in ionization.

To quantify the magnitude of this effect, we conducted experiments with the TPC azimuthally rotated from -20° to $+10^\circ$. As shown in Fig. 14, the distribution of $\sigma_{r\phi 0}$ is presented as a function of the measured local ϕ within each pad-row on the central module. Different colors represent various ϕ settings. Given the fan-shaped structure of the readout pad-row on the module, the measured ϕ values vary depending on the location of the pad-row within the module.

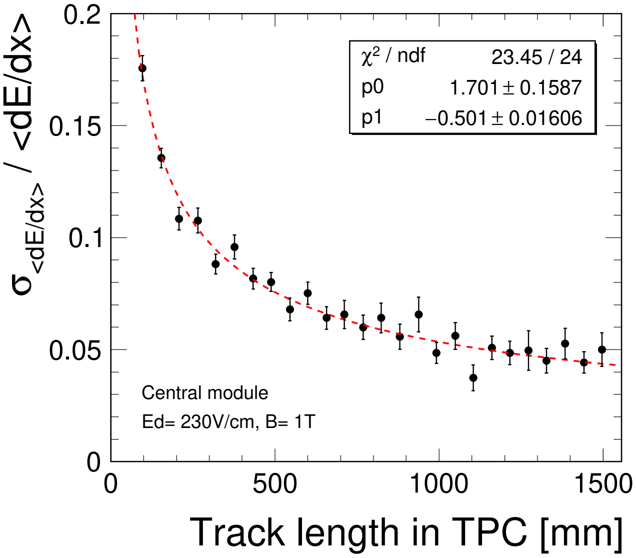

Figure 13: The dE/dx resolution as a function of the track length. The red line represents a power law fit to the data.

In reference Kobayashi et al. (2014a), the spatial resolution for inclined tracks is thoroughly examined. The constant term of the spatial resolution σ_{X0} is influenced by two factors: the intrinsic resolution for tracks parallel to the readout pad-row and the contribution from the track angle effect, expressed as

$$\sigma_{r\phi 0}^2 = \sigma_{r\phi 00}^2 + \frac{h^2 \cdot \tan^2\phi}{12} \cdot \frac{\cos\phi}{\hat{N}_{\text{eff}}} \tag{4}$$

Here, $\sigma_{X_{00}}$ represents the intrinsic resolution, parameterized by several contributions (refer to Kobayashi et al. (2014b)), including the charge dispersion in the case of a resistive anode. The variables h and ϕ denote the pad height and azimuthal angle with respect to the normal to the pad row. $\hat{N}$eff stands for the effective number of clusters collected by a specific pad row over the pad height, distinct from the effective number of electrons Neff characterizing ionization fluctuations (Eq.eq420). It's crucial to note that $\hat{N}_{\text{eff}}$ is anticipated to be independent of the drift distanceYonamine et al. (2014).

The measured points closely align with the expected function across variations in the pad-row locations. The estimated parameters, σ_{00} and $\hat{N}$eff, are $79.3 \pm 0.3\mu$m and 4.80 ± 0.04, respectively, considering a measured drift length of about 50 ± 4 mm.

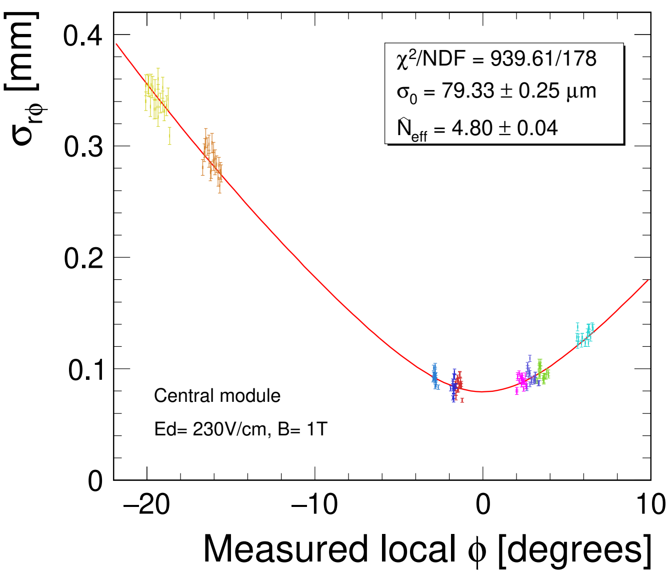

Figure 14: The rϕ resolution plotted against the measured local ϕ relative to the normal to the pad row. Each color represents data obtained at a specific TPC angle setting. Each data point corresponds to a distinct pad row, with a fixed drift distance of 50 mm.

Given a readout pad height of 7.0mm, the anticipated effective number of clusters is approximately 5.1, assuming a Polya function parameter of 0.5 Kobayashi et al. (2014b). The measured $\hat{N}$eff of 4.80 closely aligns with the expected value mentioned in the paper, and the σ_{00} of 79.3 μm is also in close agreement with the measured spatial resolution for parallel tracks along the pad-row direction.

4.7. Systematic uncertainty

The systematic uncertainty originating from the track reconstruction chain was explored by varying the reconstruction parameters essential for hit and track reconstruction. The observed relative variation in detector performance, including rϕ and z resolutions, was found to be approximately 0.6 %. This minimal fluctuation allows us to consider the resulting systematic uncertainty from the reconstruction chain as negligible. It is worth noting that the dominant contributors to the systematic uncertainty in the detector performance are the track selection criteria and module-to-module differences arising from the inhomogeneity of the charge spread, as discussed in the following section.

The inclined track rejection cut is pivotal in assessing overall performance, as a stringent cut ensures the extraction of high-momentum tracks exclusively. To estimate the robustness of this cut, we expanded the accepted window from 2.5 to 5.0 σ. We found that the fluctuation attributed to this cut remains below 2.0

4.8. Extrapolation of point resolution to MIPs in the ILD configuration

Figure 15 illustrates the extrapolation of the point resolution in $r\phi$ to a magnetic field of 3.5 T and a drift length of 2.35 m, as anticipated for the ILD detector. The extrapolation relies on a simple empirical function from equation 3, with values for $\sigma_{\mathrm{r}\phi 0}$ and N_{eff} obtained from the fit to the measured resolution. The transverse diffusion constant at 3.5 T is determined using a Magboltz simulation. The 1σ error bands are determined by the uncertainties in the fit parameters, i.e N_{eff} varies from 22 to 28 for the fitted value of 24.7. It is evident that achieving the necessary point resolution of 100 μm across the entire drift length in the ILD TPC is feasible when stringent control is maintained over gas quality, and impurities are minimized

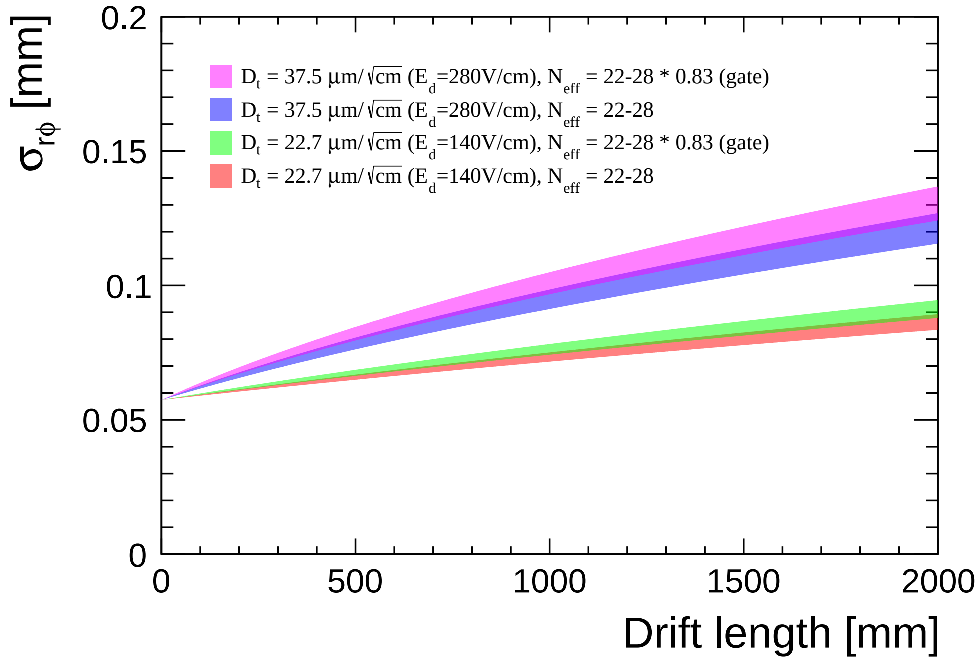

Figure 15: The extrapolation of the performance based on the simple empirical formula. Neff:22-28 is assumed for MIP.

5. Conclusion

Tests were conducted on a Time Projection Chamber (TPC) prototype equipped with Micromegas detectors, utilizing a resistive anode for efficient charge sharing among pads. To address field distortions, reduce electronic noise, and enhance gas gain flexibility, a novel high-voltage scheme was proposed. This scheme involves encapsulating the anode and setting it at a positive high voltage, while grounding the amplification mesh.

This paper presents the comprehensive test results of the Encapsulated Resistive-Anode Micromegas detector, performed with a 5 GeV electron beam, demonstrating an excellent resolution. The data obtained with the encapsulated resistive anode and the grounded mesh showcased a remarkable one-order-of-magnitude reduction in track distortions in both rϕ and z compared to the standard scheme. Rigorous control of the production process is essential to ensure detector performance.

To extrapolate the resolution in high fields, a simulation was conducted. The simulation reasonably reproduced data taken under a 1T magnetic field and predicted a spatial resolution of around 100μm at a drift length of 2m in a 3.5T magnetic field.

In conclusion, the Encapsulated Resistive-Anode Micromegas detector meets the performance requirements for the central tracker of ILD.

Acknowledgment

The authors would like to thank Rui de Oliveira and Olivier Pizzirusso from CERN for manufacturing the detectors, and acknowledge discussions with, and comments from, LCTPC collaboration members.

This work was partially supported by an International Center for Elementary Particle Physics (ICEPP) fellowship in 2018.

The measurements leading to these results have been performed at the DESY II Test Beam Facility at DESY Hamburg (Germany), a member of the Helmholtz Association (HGF). Part of this research was supported by the H2020 project AIDA-2020 under grant agreement number 654168.

References

, . Homepage of the AIDA project, (Online; accessed 20-November-2020) (2020). URL (http://https://aida-old.web.cern.ch/index.html).

, . Homepage of the DESY II testbeam facility, (Online; accessed 20-November-2020) (2020). URL (http://www.testbeam.desy.de).

, . Homepage of the EUDET project, (Online; accessed 20-November-2020) (2020). URL (http://www.eudet.org).

, . Homepage of the LCTPC collaboration, Online: accessed 20-November-2020 (2020). URL: http://www.lctpc.org.

Ackermann, K., et al., 2010. Cosmic ray tests of the prototype tpc for the ilc experiment. Nucl. Instrum. Meth. A623, 141–143. doi:10.1016/j.nima.2010.02.175.

Arogancia, D., et al., 2009. Study in a beam test of the resolution of a micromegas tpc with standard readout pads. Nucl. Instrum. Meth. A602, 403–414. doi:10.1016/j.nima.2009.01.014.

Attie, D., et al., 2017. A time projection chamber with gem-based readout. Nucl. Instrum. Meth. A856, 109–118. doi:10.1016/j.nima.2016.11.002.

Behnke, T., et al., 2010. A lightweight field cage for a large tpc prototype for the ilc. JINST 5, P10011. doi:10.1088/1748-0221/5/10/P10011.

Behnke, T., et al., 2020. The ild concept group. international large detector: Interim design report. ArXiv e-prints 2003.01116.

Bhattacharya, D., Date: 10/12/2015. Study of a multi-module MicromegasTPC prototype for tracking at the International Linear Collider, (Online; accessed 20-November-2020) (2020). URL (http://irfu.cea.fr/Spp/ILC-TPC/home/talks/2015/151210_D.S.Bhattacharya_PreThes Jadavpur University, Kolkata.

Bhattacharya, D.S., Date: 26/03/2015. Results of Test Beam 2015, (Online; accessed 20-November-2020) (2020). URL (http://irfu.cea.fr/Spp/ILC-TPC/home/talks/2015/150326_D.S.Bhattacharya_MM_Anal Micromegas Analysis Meeting.

Biagi, S.F., 1999. Monte Carlo simulation of electron drift and diffusion in counting gases under the influence of electric and magnetic fields. Nucl. Instrum. Meth. A421, 234–240. doi:10.1016/S0168-9002(98)01233-9.

Blobel, V., 2006. Software alignment for tracking detectors. Nucl. Instrum. Meth. A566, 5–13. doi:10.1016/j.nima.2006.05.157.

Colas, P., et al., 2004. The readout of a gem or micromegas-equipped tpc by means of the medipix2 cmos sensor as direct anode. Nucl. Instrum. Meth. A535, 506–510. doi:10.1016/j.nima.2004.07.180.

Dixit, M., et al., 2004. Position sensing from charge dispersion in micro-pattern gas detectors with a resistive anode. Nucl. Instrum. Meth. A518, 721–727. doi:10.1016/j.nima.2003.09.051.

Gaede, F., 2006. Marlin and LCCD: Software tools for the ILC. Nucl. Instrum. Meth. A559, 177–180. doi:10.1016/j.nima.2005.11.138.

Gaede, F., et al., 2003. LCIO: A Persistency framework for linear collider simulation studies. ArXiv e-prints: physics 0306114.

Giomataris, Y., et al., 1996. Micromegas: A high granularity position sensitive gaseous detector for high particle flux environments. Nucl. Instrum. Meth. A376, 29–35. doi:10.1016/S0168-9002(98)01233-9.

Kleinwort, C., a. General Broken Lines wiki page, (Online; accessed 20-November-2020) (2020). URL (https://www.terascale.de/wiki/generalbrokenlines/).

Kleinwort, C., b. Millepede II wiki page, (Online; accessed 20-November-2020) (2020). URL (https://www.wiki.terascale.de/index.php/Millepede_II).

Kleinwort, C., 2012. General Broken Lines as advanced track fitting method. Nucl. Instrum. Meth. A673, 107–110. doi:10.1016/j.nima.2012.01.024.

Kleinwort, C., 2014. A Track Finding Method for a TPC Based on Triplet Chains. Technical Report. LC Notes, LC-TOOL-2014-004. https://bib-pubdb1.desy.de/record/193045.

Kobayashi, M., 2006. An estimation of the effective number of electrons contributing to the coordinate measurement with a TPC. Nucl. Instrum. Meth. A562, 136–140. doi:10.1016/j.nima.2006.03.001.

Kobayashi, M., et al., 2014a. Cosmic ray tests of a GEM-based TPC prototype operated in Ar-CF_4–isobutane gas mixtures: II. Nucl. Instrum. Meth. A767, 439–444. doi:10.1016/j.nima.2014.08.027.

Kobayashi, M., et al., 2014b. Cosmic ray tests of a GEM-based TPC prototype operated in Ar–CF4–isobutane gas mixtures. Nucl. Instrum. Meth. A764, 394. doi:10.1016/j.nima.2014.07.050.

Kraemer, T., 2006. Track Parameters in LCIO. Technical Report. LC Notes, LC-DET-2006-004. http://bib-pubdb1.desy.de/record/81214.

Mueller, F.J., 2016. Development of a Triple GEM Readout Module for a Time Projection Chamber and Measurement Accuracies of Hadronic Higgs Branching Fractions in $\nu\nu H$ at a 350 GeV ILC. Ph.D. thesis. University Hamburg. URL (https://bib-pubdb1.desy.de/record/301339).

Sauli, F., 1997. Gem: A new concept for electron amplification in gas detectors. Nucl. Instrum. Meth. A386, 531–534. doi:10.1016/S0168-9002(96)01172-2.

Shiell, N.M., 2012. A New Analysis Technique to Improve Spatial Resolution for a Resistive Anode Time Projection Chamber. Master's thesis. Carleton University (Canada). URL (https://ui.adsabs.harvard.edu/abs/2012MsT.........30S/abstract).

Shoji, A., 2018. Measurement of dE/dx resolution of TPC prototype with gating GEM exposed to an electron beam. ArXiv e-prints 1801.04499.

Veenhof, R. Schindler, H., . Garfield++ – simulation of tracking detectors, (Online; accessed 20-November-2020) (2020). URL (https://garfieldpp.web.cern.ch/garfieldpp/support/).

Vogel, A., et al., 2007. MarlinTPC: A Marlin based common TPC software for the LC-TPC Collaboration. Technical Report. LC Notes, LC-TOOL-2007-001. http://bib-pubdb1.desy.de/record/83142.

Wang, W., 2013. A Large Area Micromegas TPC for Tracking at the ILC. Ph.D. thesis. Université Paris Sud - Paris XI. URL (https://tel.archives-ouvertes.fr/tel-00854414/document).

Yonamine, R., et al., 2014. Spatial resolutions of GEM TPC. A novel theoretical formula and its comparison to latest beam test data. JINST 9, C03002. doi:10.1088/1748-0221/9/03/C03002.

Zerguerras, T., et al., 2015. Understanding avalanches in a Micromegas from single-electron response measurement. Nucl. Instrum. Meth. A772, 76–82. doi:10.1016/j.nima.2014.11.014.